Numerical study of fillet welds subjected to quasi-static and impact loading

Erik Løhre Grimsmo[a,*], Lars Edvard Bryhni Dæhli[a], Odd Sture Hopperstad[a], Arne Aalberg[a,b], Magnus Langseth[a], Arild Holm Clausen[a]

[a]*Structural Impact Laboratory (SIMLab), Centre for Advanced Structural Analysis (CASA), Department of Structural Engineering, Norwegian University of Science and Technology (NTNU), NO-7491, Trondheim, Norway*
[b]*The University Centre in Svalbard*

Abstract

Fillet welding is widely used in connections in civil engineering and marine structures. Thus, understanding the behaviour of fillet welds under various types of loading is important, and numerical simulations can provide increased insight into this topic. This paper concerns finite element simulations of previous quasi-static and dynamic (impact) tests on fillet welds. The test specimens employed were structural steel components joined by either longitudinally or transversely oriented fillet welds. In the simulations, the material of the fillet welds was modelled using a shear-modified Gurson model, which accounts for material softening in both low and high stress triaxiality regimes. Additionally, strain rate and temperature dependencies were incorporated in the material model with a modified Johnson-Cook constitutive relation for the matrix material. Several types of material tests were conducted to identify the parameters entering the material model. For the quasi-static component tests and simulations, a good agreement was observed in terms of both force-deformation curves and failure mechanisms. The simulations of the dynamic tests predicted appreciably higher force levels and weld deformations at failure than those obtained in the corresponding experiments. A parameter study showed that these discrepancies may partly be due to inaccurate values used for the material parameters related to strain-rate hardening and thermal softening. Finally, a comparison was made between simulations with the shear-modified Gurson model and a simpler material model that does not account for void-induced softening. The simpler model employed the Cockcroft-Latham failure criterion, uncoupled from the constitutive relations. This model was unable to capture the response of the fillet welds to the same extent as

the shear-modified Gurson model.
Keywords: Fillet welds, finite element simulations, impact loading, shear-modified Gurson, Johnson-Cook

1. Introduction

Fillet welds are common connection elements in structural joints such as beam-to-column joints. A vast amount of experimental data concerning fillet welds under quasi-static load conditions can be found in the literature, as the literature review by Miazga and Kennedy (1989) shows. However, hardly any studies are concerned with the behaviour of fillet welds under severe impulsive loading. Grimsmo et al. (2017) therefore performed experiments where fillet welds of steel were subjected to quasi-static and impact loading. The test specimens had fillet welds oriented either longitudinally or transversely to the load direction. It was experienced that the resistances of the welds were practically unaffected by the deformation rate. The deformation capacity, i.e., deformation before fracture, of the transverse welds was also independent of the deformation rate. On the other hand, the longitudinal welds experienced a significant reduction in the deformation capacity as the deformation rate was increased. The principal purpose of the present work is to investigate whether the behaviour observed in these quasi-static and dynamic tests can be captured with finite element (FE) simulations. Moreover, the simulations are employed to study strain rate and thermal effects in the dynamic tests. The simulations of the quasi-static and dynamic tests are hereafter denoted the quasi-static and dynamic simulations, respectively.

In the past decades, efforts have been made to model fillet welds subjected to quasi-static loading by means of FE simulations. One major advantage of simulations compared to experiments is the low economical cost. Thus, parametric and sensitivity studies are cheap to perform. Furthermore, the inevitable scatter of results obtained from physical tests of welds is avoided with FE simulations, which makes it simpler to isolate and investigate the effects of varying parameters. Numerical simulations also conveniently allow for studying local mechanisms such as the evolution of plastic strain and damage in the deforming welds. Many of the FE models of fillet welds in

*Erik Løhre Grimsmo
Email address: erik.l.grimsmo@ntnu.no (Erik Løhre Grimsmo)

the literature, where the geometry of the welds is explicitly modelled, are two-dimensional (2D) and employ plain strain elements; see for instance Kanvinde et al. (2008, 2009), and Picòn and Cañas (2009). As the number of elements is significantly lower for 2D models than for comparative 3D models, finer element meshes can be used. However, 2D models cannot account for out-of-plane deformations, which restricts the analyses to simulate fillet welds loaded transversely to the length axis of the weld. To accommodate more general loading conditions, we employed 3D models in the present work.

An adequate material model is a necessary prerequisite for capturing the behaviour observed in the tests. This implies that the material model should incorporate yielding, work hardening, strain-rate hardening, thermal softening, and damage softening. Kanvinde et al. (2008) employed a micromechanical model called the Stress Modified Critical Strain (SMCS) model to predict fracture in FE simulations of fillet welds under quasi-static loading. By comparing the simulations with corresponding tests, as well as simulations with a traditional fracture model based on the J-integral, they observed that the SMSC model was better suited to predict fracture than the J-integral model. Nielsen and Tvergaard (2010) applied a shear-modified Gurson model similar to the one proposed by Nahshon and Hutchinson (2008) to simulate failure of spot welds of steel. However, Nielsen and Tvergaard (2010) argued that the damage contribution from the shear modification is possibly too large for moderate and high stress triaxiality states where effects of the third deviatoric stress invariant are less significant. They therefore modified the shear contribution to be a function of stress triaxiality so that it vanishes at high stress triaxialities. From their simulations of shear and plug failure of spot welds, they observed that this modification allowed the shear-modified Gurson model to be used for both low and high stress triaxiality regimes.

In the present work, we employ a shear-modified Gurson model similar to the one used by Nielsen and Tvergaard (2010). However, two modifications are incorporated. First, the yield function of the matrix material is described by the general isotropic yield criterion proposed by Hershey (1954) rather than the von Mises yield criterion. Thus, effects of the third deviatoric stress invariant are incorporated in the yield criterion. Second, the shear damage contribution is governed by a slightly different function of triaxiality. Strain-rate and temperature sensitivity are introduced in the material model by assuming that the flow stress of the matrix material follows a modified Johnson-Cook constitutive relation similar to the one proposed by Børvik et al. (2001).

We have performed a comprehensive set of material tests to determine several of the parameters employed in the material model. These experiments included tensile tests with smooth specimens conducted at different strain rates, tensile tests with notched specimens, and shear tests with in-plane shear specimens. The material test programme incorporated both the fillet weld material and the base material around the welds, but the main focus was on the weld material. Note that welding-induced residual stresses are not considered in the present work.

The paper is organised as follows. Section 2 presents both the component tests and the material tests. The material model and the calibration of material parameters from the material tests are discussed in Section 3. Section 4 presents the FE model of the components tests, and the corresponding simulation results are provided in Section 5. Finally, some concluding remarks are presented in Section 6.

2. Laboratory tests

2.1. Component tests

Grimsmo et al. (2017) provide a detailed description of the component test specimens and setup, and only a summary is therefore presented herein.

Figure 1 depicts the two types of component test specimens employed; one with four fillet welds oriented longitudinally with respect to the load direction and one with two fillet welds oriented transversely with respect to the load direction. The specimens are denoted longitudinal and transverse specimen, respectively. Both specimen types comprise two plates with dimensions $230 \times 160 \times 15$ mm^3 that were fillet welded to a brick with dimensions $60 \times 60 \times 30$ mm^3. These parts were made of S355 steel, whereas the specified minimum yield stress was 460 MPa for the basic-coated stick electrodes used to assemble the specimens. The specified throat thickness of the fillet welds was 4 mm, and the lengths of the welds were 30 and 60 mm for the longitudinal and transverse specimens, respectively. This design of the specimens ensured that plastic deformations and failure predominantly occurred in the fillet welds, and not in the adjacent base material. Thus, the strength and ductility of the welds can be determined, which is essential knowledge in design of welded components and structures.

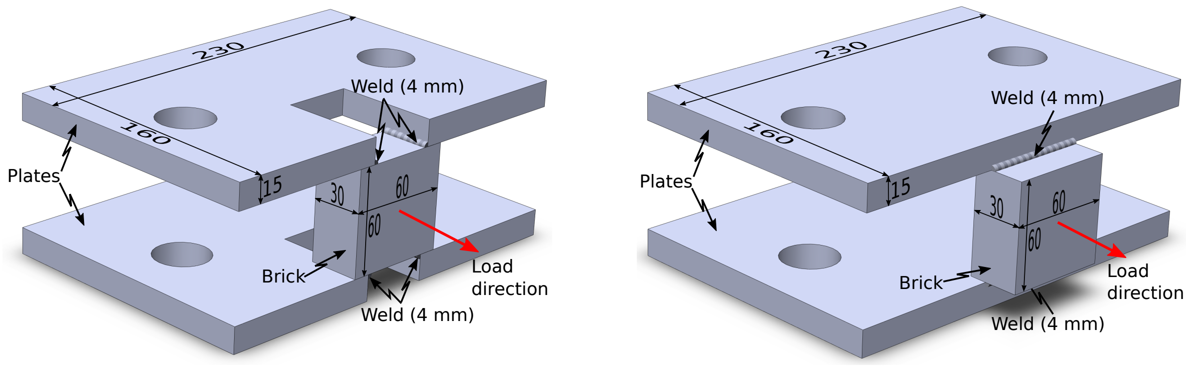

(a) The longitudinal specimen, which has four fillet welds

(b) The transverse specimen, which has two fillet welds

Figure 1: Illustrations of the component test specimens (dimensions in mm).

The specimens were mounted in a fixture, as shown in Figure 2. The fixture consisted of two supporting blocks that were welded to a supporting plate and bolted to the stationary part of the test machines. Two M30 bolts of grade 12.9, which were finger-tightened, fixed the specimens to the supporting blocks. The so-called nose in Figure 2 was welded to a circular plate that was attached to the moving part of the test machines. During a test, the nose displaced along its longitudinal axis and between the supporting blocks. As the nose attained contact with the brick of the test specimens, the fillet welds became loaded. Since the plates of the specimens were practically fixed, the fillet welds were deformed and eventually failed. The strain gauges attached to the nose (see Figure 2) enabled determining the axial force developing in the nose.

The quasi-static tests were carried out with a standard servo-hydraulic test machine, and the applied displacement rate was approximately 0.5 mm/min. A pendulum accelerator was employed in the dynamic tests. This test machine accelerated a trolley of 1444 kg, which rolled along two rails. In this experimental programme, the trolley was accelerated to a velocity of 2.3-2.5 m/s. The nose in Figure 2 was mounted on the front of the trolley, whereas the fixture and the test specimens were attached to a reaction wall. After the trolley moved a certain distance, the nose impacted the brick of the test specimens. Thus, the fillet welds experienced a high deformation rate.

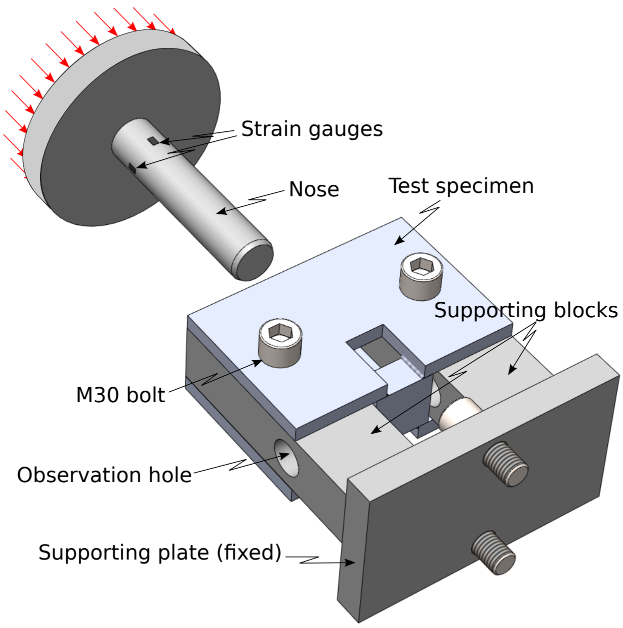

Figure 2: Illustration of the component test assembly with a longitudinal specimen mounted in the rig.

2.2. Material tests

In order to identify the parameters employed in the material model described in Section 3, we conducted a large number of material tests. Figure 3 shows the geometry and dimensions of the various material test specimens, which facilitate tensile loading with different stress triaxialities and shear loading. The comparatively small dimensions of the specimen in Figure 3a enabled extracting this specimen type from the fillet welds of the component specimens, where the tension specimens were oriented along the length of the fillet welds. However, this was a costly procedure, and only four specimens were therefore machined from the fillet welds, two from each type of component specimen, i.e., longitudinal and transverse.

The V-butt weld assembly in Figure 4 simplified testing a weld material made with the same electrode type as for the fillet welds. This assembly comprised two 16 mm steel plates placed 14 mm apart, and a 10 mm steel backing-plate spot welded to the other two plates. The 16 mm plates were bevelled so that they formed a V-shaped groove. Several passes were necessary to fill the groove with weld metal. Material test specimens of the types in Figure 3b, 3c, and 3d were machined from the butt weld, as indicated in Figure 4. Material test specimens of the type in

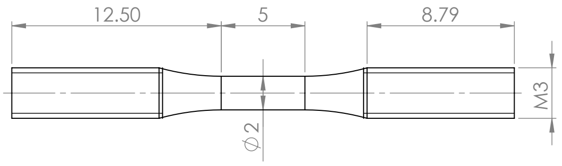

(a) Smooth tension test specimen machined from the fillet welds

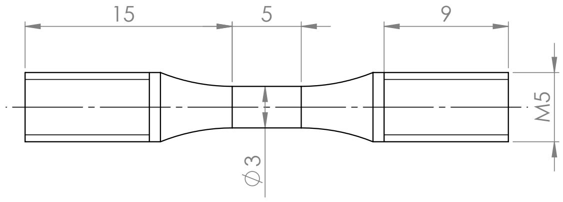

(b) Smooth tension test specimen machined from butt weld, brick, and plate material.

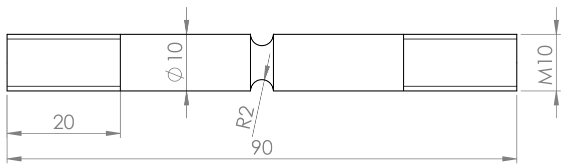

(c) Notched tension specimen machined from the butt weld.

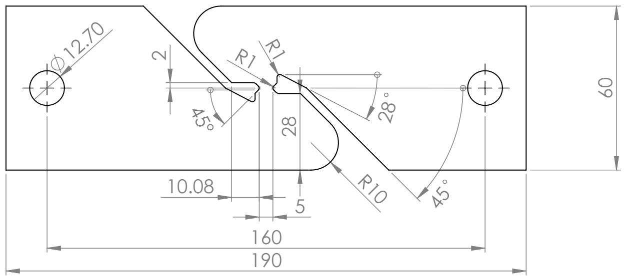

(d) In-plane shear specimen machined from the butt weld.

Figure 3: Test specimens used in the material tests.

Figure 3b were also machined from the brick and plate material.

Figure 5 displays the engineering stress-strain curves determined from tensile tests of the fillet weld material of the longitudinal and transverse specimens, the butt weld, and the base materials, i.e., the brick and plate materials. As appearing from the figure, two or three replicate tests were conducted for each case. Although the butt weld was manufactured with the same electrode type as used for the fillet welds, Figure 5 shows a difference of around 20% in strength between the materials of the butt and fillet welds. As discussed by Grimsmo et al. (2017), this observation can probably be explained by differences in cooling rates. Nevertheless, we assume in Section 3 that some of the material parameters determined from the butt weld material are representative for the fillet weld material of the component specimens.

A strain-rate sensitivity study was conducted by subjecting the tensile specimens of the type in Figure 3b to strain rates of approximately 10^{-3}, 10^{-1}, and 300 s^{-1}. The two lowest strain rates were obtained by employing a standard screw-driven test machine, whereas the highest strain rate was achieved by using a split-Hopkinson tension bar. For this investigation, the butt weld and plate

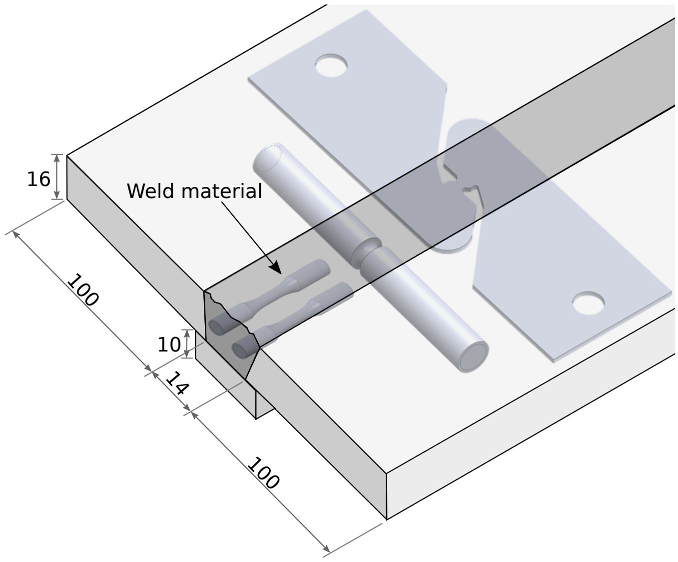

Figure 4: Illustration of the V-butt weld assembly and how the material test specimens were extracted.

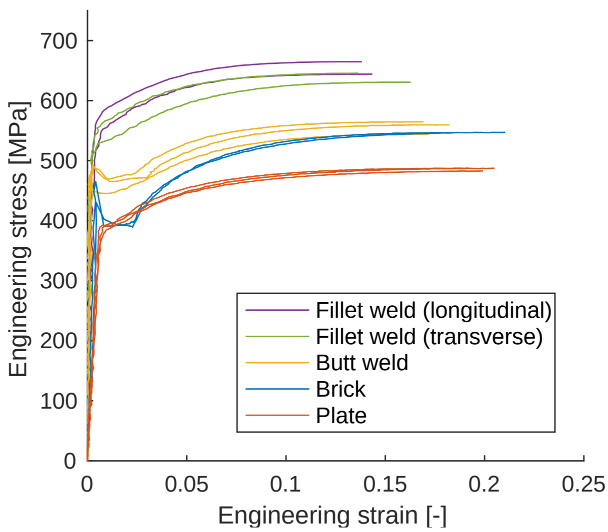

Figure 5: Engineering stress-strain curves acquired from tensile tests with smooth specimens (Reprint from Grimsmo et al. (2017)).

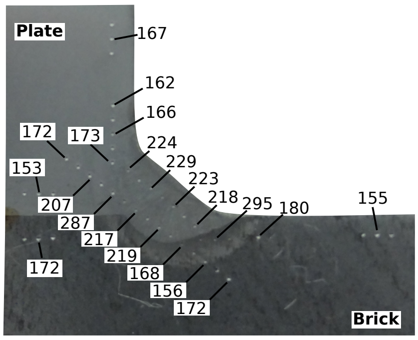

(a) Longitudinal specimen

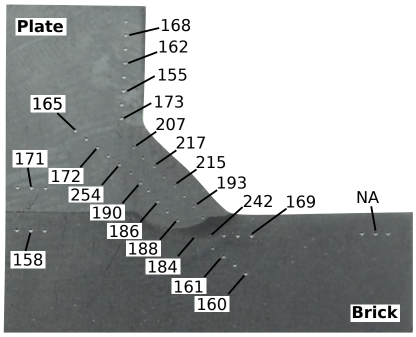

(b) Transverse specimen

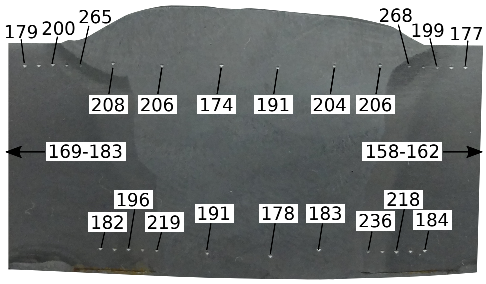

(c) Butt weld

Figure 6: Results from Vickers hardness tests performed on sections of welds (Reprint from Grimsmo et al. (2017)).

materials were tested, and the results are provided in Section 3.3.4. We assume that the strain-rate sensitivity parameters obtained for the butt weld and plate materials are also representative for the fillet weld and brick materials of the component specimens.

In addition to the tests described in the preceding paragraphs, Vickers hardness tests were carried out on polished cross-sections cut from a longitudinal and a transverse specimen, as well as the butt weld assembly. The measured hardness values are shown in Figure 6. Hardness is commonly assumed proportional to the strength. Thus, the hardness measurements agree with the results in Figure 5 since the hardness in general is significantly higher for the weld material compared to the base material. Figure 6a and 6b also show that there is a noticeable zone where the electrode and base material have fused together, which means that the effective throat thickness of the fillet welds is slightly larger than the one determined from external throat thickness measurements. This was taken into account in the FE model, as described in Section 4.3.

3. Material modelling

3.1. Background

The choice of material model was based on the following observations:

- From scanning electron microscope images (see Grimsmo et al. (2017)) it appeared that predominantly ductile fracture occurred.
- Strongly localized deformation occurred in the welds, which suggests that incorporating material softening is appropriate.
- The simulations showed that both the stress triaxiality and Lode angle varied considerably within the failure plane of the welds. Thus, both the stress triaxiality and Lode angle dependence of the failure strain should be considered.
- The duration of the impact tests was of the order of 1 millisecond. Thus, high strain rates were present and strain-rate hardening should therefore be accounted for. Moreover, such short test durations justify the assumption of adiabatic heating because heat conduction and convection effects can be neglected.
- Results from microhardness tests suggested that some thermal softening took place (see Grimsmo et al. (2017)). Moreover, infrared-camera measurements indicated that significant heating took place in the welds. Thermal softening should therefore be included.

Ductile failure is governed by the growth and coalescence of microscopic voids that are either present in the material prior to deformation or nucleate from particles during the course of the deformation, as discussed by for instance Garrison and Moody (1987). A widely used model was proposed by Gurson (1977), who performed an upper-bound plastic limit analysis of a hollow sphere. His seminal porous plasticity model has later found extensive use throughout the literature. However, an inherent limitation of the Gurson model resides in the assumption of a spherical volume element, which restricts the void growth to remain spherical, and thus renders the model incompatible with the void evolution typically observed under low and moderate stress triaxialities. This has important consequences for the numerical modelling of structural components, where a large range of stress triaxialities are present. Possible ways to overcome this deficiency were proposed by Nahshon and Hutchinson (2008) and Xue (2008) by augmenting the rate of void growth with a term that accounts for the deviatoric part of the plastic strain rate. By way of consequence, such an extension incorporates damage due to shearing and rotation of the voids.

Steels usually display yield surfaces that depend upon the position in the deviatoric stress plane. We therefore extended the Gurson model to incorporate effects of the third principal invariant of the stress deviator (J_3). Moreover, steels subjected to fast transient dynamics normally exhibit considerable strain-rate hardening and thermal softening effects. Johnson and Cook (1983) proposed an empirical-based constitutive relation suitable for such conditions. A modified version of this extensively used relation is therefore also adopted in the current work.

3.2. Material model description

The constitutive model is implemented in the finite element framework using a corotated formulation, such that

$$\hat{\boldsymbol{\Sigma}} = \mathbf{R}^{\mathrm{T}} \cdot \boldsymbol{\Sigma} \cdot \mathbf{R} \tag{1a}$$

$$\hat{\mathbf{D}} = \mathbf{R}^{\mathrm{T}} \cdot \mathbf{D} \cdot \mathbf{R} \tag{1b}$$

where the superimposed hat notation is used to represent the corotated tensors. The rotation tensor $\mathbf{R}$ is defined through the polar decomposition of the deformation gradient, $\boldsymbol{\Sigma}$ is the Cauchy stress tensor at the homogenized material level, and $\mathbf{D}$ is the rate-of-deformation tensor. We assume that the rate-of-deformation tensor can be split into elastic and plastic parts, viz.

$$\hat{\mathbf{D}} = \hat{\mathbf{D}}^{\mathrm{e}} + \hat{\mathbf{D}}^{\mathrm{p}} \tag{2}$$

The elastic response is governed by the linear Hooke's law on rate form

$$\dot{\hat{\boldsymbol{\Sigma}}} = \frac{E}{1+\nu}\hat{\mathbf{D}}'^{\mathrm{e}} + \frac{E}{3\,(1-2\nu)}\mathrm{tr}\,(\hat{\mathbf{D}}^{\mathrm{e}})\mathbf{1} \tag{3}$$

where E and ν are the elastic constants, $\mathbf{D}'^{\mathrm{e}}$ and $\mathrm{tr}\,(\mathbf{D}^{\mathrm{e}})$ are the deviatoric and volumetric parts of the elastic rate-of-deformation tensor, respectively, and $\mathbf{1}$ is the second-order identity tensor. We note that thermoelasticity is not considered, and that any influence of the voids on the elastic response is neglected. This is deemed acceptable since the elastic deformations and the porosity are predominantly small throughout the loading.

To enable the description of material damage, we have employed a heuristic extension of the porous plasticity model derived by Gurson (1977). This extension follows along the same lines as taken by Doege and Seibert (1995) in the case of a Hill (1948) plastically anisotropic matrix formulation. The yield function reads

$$\Phi\left(\hat{\boldsymbol{\Sigma}}, f, \sigma_M\right) = \left(\frac{\Sigma_{\mathrm{eq}}}{\sigma_{\mathrm{M}}}\right)^2 + 2q_1 f \cosh\left(\frac{3}{2}q_2\frac{\Sigma_{\mathrm{h}}}{\sigma_{\mathrm{M}}}\right) - 1 - (q_1 f)^2 \leq 0 \tag{4}$$

where Σ_{eq} and Σ_{h} are the equivalent and hydrostatic stress measures derived from the Cauchy stress tensor $\hat{\boldsymbol{\Sigma}}$, σ_{M} is the matrix flow stress, f is the void volume fraction, and q_1 and q_2 are the material parameters introduced by Tvergaard (1981). We use the values suggested by Tvergaard (1981) throughout this paper, and thus $q_1 = 1.5$ and $q_2 = 1.0$. The yield function is slightly modified by using an equivalent stress measure on the form given by Hershey (1954), namely

$$\Sigma_{\mathrm{eq}} = \left[\frac{1}{2}\left(|\Sigma_1 - \Sigma_2|^a + |\Sigma_2 - \Sigma_3|^a + |\Sigma_3 - \Sigma_1|^a\right)\right]^{\frac{1}{a}} \tag{5}$$

where Σ_1, Σ_2, and Σ_3 are the principal values of $\hat{\boldsymbol{\Sigma}}$ and the coefficient a governs the curvature of the yield surface in the deviatoric stress plane. The current porous plasticity model thus accounts for effects of J_3 whenever $a \neq \{2, 4\}$. An exponent value of $a = 6$ is typically assumed for metals with a body-centred cubic (BCC) crystal structure; see for instance Hosford and Caddell (1993). We therefore use $a = 6$ in the current study.

The matrix material is defined as elastic-thermoviscoplastic with isotropic work hardening governed by a two-term Voce hardening rule. Strain-rate hardening and thermal softening are accounted for in the matrix material through a modified Johnson-Cook constitutive relation similar to the one proposed by Børvik et al. (2001), viz.

$$\sigma_{\mathrm{M}} = \left[\sigma_0 + \sum_{i=1}^{2} Q_i\left(1 - \exp\left(-\frac{\theta_i}{Q_i}p\right)\right)\right]\left[1 + \frac{\dot{p}}{\dot{p}_0}\right]^c\left[1 - \left(\frac{T - T_a}{T_m - T_a}\right)^m\right] \tag{6}$$

where σ_0 is the initial yield stress, Q_i and θ_i are constants describing the level and rate of strain hardening, p is the equivalent plastic strain, $\dot{p}$ and $\dot{p}_0$ are the equivalent plastic strain rate and the reference plastic strain rate, c is the rate sensitivity parameter, T is the current temperature, T_m and T_a are the melting and ambient temperatures, and m is a constant governing thermal softening.

The associated flow rule is adopted, such that

$$\hat{\mathbf{D}}^{\mathrm{p}} = \dot{\Lambda}\frac{\partial \Phi}{\partial \hat{\mathbf{\Sigma}}} \tag{7}$$

where $\dot{\Lambda}$ serves as the plastic multiplier. The plastic strain rate $\dot{p}$ is defined as the plastic power conjugate measure to the flow stress σ_M, and in association with the Gurson model it is calculated from

$$\dot{p} = \frac{\hat{\mathbf{\Sigma}} : \hat{\mathbf{D}}^{\mathrm{p}}}{(1-f)\,\sigma_{\mathrm{M}}} \tag{8}$$

The total increase of the void volume fraction is governed by two contributions

$$\dot{f} = \dot{f}_{\mathrm{g}} + \dot{f}_{\mathrm{s}} \tag{9}$$

in which $\dot{f}_{\mathrm{g}}$ denotes growth of voids due to matrix incompressibility (Gurson, 1977) and $\dot{f}_{\mathrm{s}}$ accounts for damage due to shearing of voids (Nahshon and Hutchinson, 2008). Specifically, the two void growth terms are given by

$$\dot{f}_{\mathrm{g}} = (1-f)\,\mathrm{tr}\,(\hat{\mathbf{D}}^{\mathrm{p}}) \tag{10a}$$

$$\dot{f}_{\mathrm{s}} = (1-\cos^2(3\theta))k_{\mathrm{s}}^{*} f \frac{\hat{\mathbf{\Sigma}}' : \hat{\mathbf{D}}^{\mathrm{p}}}{\Sigma_{\mathrm{eq}}} \tag{10b}$$

where k_s^* is a parameter defined below and θ is the Lode angle, which is defined as

$$\cos 3\theta \equiv \frac{J_3}{2\sqrt{(J_2/3)^3}} \tag{11}$$

Here J_2 is the second principal invariant of the stress deviator. The initial void volume fraction, i.e., $f(t=0) = f_0$, serves as an initial condition for Equation (9). Due to the inclusion of the shear term in this equation, the void volume fraction f should be regarded as a damage parameter since the mass balance of the underlying representative volume element is violated, as discussed by Nahshon and Hutchinson (2008). In the FE element simulations, the elements are deleted as the void volume fraction f reaches its critical value f_c at the integration points.

Inspired by the modification presented in the study by Nielsen and Tvergaard (2010), we have suitably modified the parameter k_{s}^* such that the shear term is scaled by the stress triaxiality σ^*, which is given by the expression

$$\sigma^* = \frac{\Sigma_{\mathrm{h}}}{\sqrt{3J_2}} \tag{12}$$

In the current study, we employ a continuous function to scale the shear term with stress triaxiality according to

$$k_{\mathrm{s}}^{*} = \left(\frac{1}{1 + \langle \sigma^{*} - \sigma_{0}^{*} \rangle^{s}} \right) k_{\mathrm{s}} \tag{13}$$

where k_s and s are constants, σ_0^* is a reference triaxiality level which shifts the scaling curve along the σ^*-axis, and the Macaulay bracket $\langle x \rangle = \max(0, x)$ is used to enforce positive scaling for all triaxialities. The purpose of the function in Equation (13) is to reduce the shear damage contribution given in Equation (10b) for moderate and high stress triaxialities; see Section 3.3.3 for more details.

The loading/unloading conditions are governed by the Kuhn-Tucker expressions, i.e.,

$$\Phi \leq 0, \quad \dot{\Lambda} \geq 0, \quad \Phi\dot{\Lambda} = 0 \tag{14}$$

where $\Phi = 0$ represents a so-called dynamic yield surface; see for instance Ristinmaa and Ottosen (2000).

The temperature change under adiabatic conditions is calculated using

$$\dot{T} = \frac{\chi}{\rho C_p} \hat{\mathbf{\Sigma}} : \hat{\mathbf{D}}^{\mathrm{p}} \tag{15}$$

where χ is the Taylor-Quinney coefficient, which determines the fraction of plastic work converted to heat, ρ is the density, and C_p is the specific heat capacity.

A semi-implicit return map algorithm was used for temporal integration of the governing equations. If the equivalent strain norm $||\Delta t \hat{\mathbf{D}}|| > 0.01\varepsilon_0 = 0.01\sigma_0/E$ during the return mapping, a sub-stepping algorithm was enforced to ensure sufficient accuracy.

3.3. Material parameter identification

The material parameters entering the constitutive relation and the equations governing the increase of void volume fraction were determined from a series of material tests and by inverse modelling of these tests. The tests were presented in Section 2.2. Inspired by the work of Xue et al. (2010, 2013), we employed a calibration procedure which is summarized as follows:

- The matrix flow stress parameters were determined by employing the smooth tensile specimens (see Section 3.3.1)

- The initial porosity was estimated by using the notched tensile specimens in which the triaxiality is high (see Section 3.3.2)

- The shear damage parameters were found by employing the in-plane simple shear specimens (see Section 3.3.3).

Note that the first bullet point above pertains to all the materials, i.e., the weld, plate, and brick materials. The two remaining bullet points apply only to the weld materials. More specifically, notched tensile tests and shear tests were conducted for the butt weld material, and the parameters determined for this material are also assumed to be representative for the fillet weld material. Since the plate and brick materials experienced insignificant damage in the tests, they were modelled as non-porous, which is equivalent to setting $f = 0$ in Equation (4). Thus, failure in the base material was not considered herein. To further reduce the computational effort, the plate and brick materials were modelled using the von Mises yield criterion, which corresponds to setting $a = 2$ in Equation (5). For the weld materials, on the other hand, $a = 6$ was assumed. Section 3.3.4 describes how the strain-rate sensitivity parameters were determined from smooth tensile tests conducted under low, medium, and high strain rates.

Table 1 lists the material parameters identified for the fillet weld material, as well as for the plate and brick materials. In addition to the material parameters given in this table, several other parameters were employed in the simulations. Ordinary values for steel were assumed for the following parameters: $E = 210$ GPa, $\nu = 0.33$, $\rho = 7800$ kg/m^3, and $C_p = 452$ J/kgK. The temperature related parameters in Equation (6) were chosen based on the work by Dey et al. (2004). They tested three Weldox steels of different strengths, and found that m varied between approximately 0.9 and 1.1 for the different steels. We therefore adopted $m = 1.0$ in the present work, whereas the ambient temperature T_a and melting temperature T_m were taken as 293 and 1800 K, respectively.

3.3.1. Matrix yield and work hardening parameters

This section only shows the results obtained from tests and simulation of the butt weld material. However, the same procedure was used for the fillet weld, plate, and brick materials. Furthermore,

Table 1: Material parameters identified from material tests and simulations

Parameter	**Weld**	**Plate**	**Brick**
σ_0 [MPa]	550.0	384.0	397.0
Q_1 [MPa]	132.8	97.1	180.8
θ_1 [MPa]	2806	1991	4215
Q_2 [MPa]	351.2	379.6	548.2
θ_2 [MPa]	565.9	621.0	564.9
f_0	0.001	0.0	0.0
f_c	0.12	-	-
k_s	4.0	-	-
σ_0^*	-0.5	-	-
s	20.0	-	-
$\dot{p}_0$ [1/s]	0.001	0.001	0.001
c	0.017	0.020	0.020

the critical void volume fraction f_c is not considered in the simulations presented in this section and in Section 3.3.2 and 3.3.3. All simulations presented in this paper were performed by employing the commercial FE software Abaqus/Explicit.

As mentioned previously, the tests and subsequent FE simulations with smooth tensile specimens were conducted to determine the yield and work-hardening parameters of the two-term Voce law in Equation (6). Figure 7a shows the discretized model of the tensile specimen used in the numerical simulations. Axisymmetry was assumed for computational efficiency. As the load conditions were quasi-static, the strain rate and temperature dependencies were omitted from the material model in these simulations. In order to capture the response experienced, also after necking of the specimens, the hardening parameters were optimized so that a good agreement between tests and simulation in terms of engineering stress versus diameter reduction ratio was obtained, as exemplified in Figure 8. Note that the yield plateaus observed for the test curves were accounted for in the simulation. However, distinct yield plateaus were only observed for the butt weld and

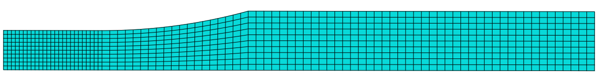

(a) Smooth tensile specimen model (axisymmetric). Element size in gauge length is 0.15 mm.

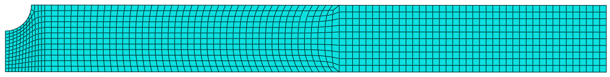

(b) Notched tensile specimen model (axisymmetric). Element size in notch region is 0.25 mm.

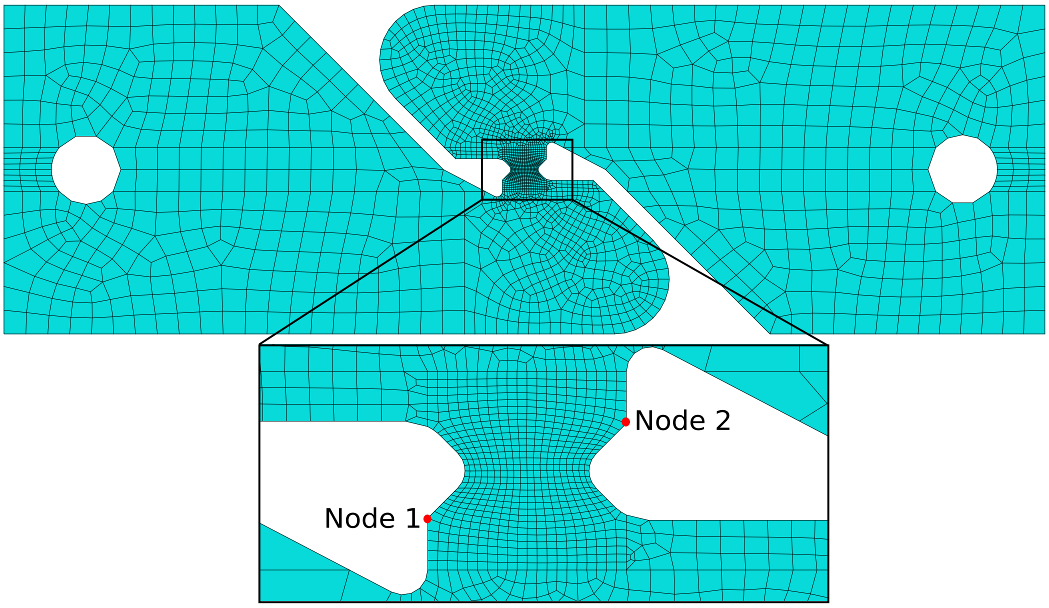

(c) Shear specimen model (3D). Element size in shear deformation zone is approximately 0.25 mm. Displacements of the two nodes highlighted with red dots were used to evaluate the deformation in the test.

Figure 7: Discretization of the material test specimens.

brick materials (see Figure 5), and were therefore not included in the material model description in Section 3.2. Note further the appreciable scatter between the three experimental curves in Figure 8, which can be expected for weld metals.

In accordance with the observations of Xue et al. (2010), we found that the material softening induced by void growth had negligible influence on the response in the simulations with smooth tensile specimens, and we thus chose to calibrate the matrix flow stress parameters by using zero initial porosity, i.e., $f_0 = 0$.

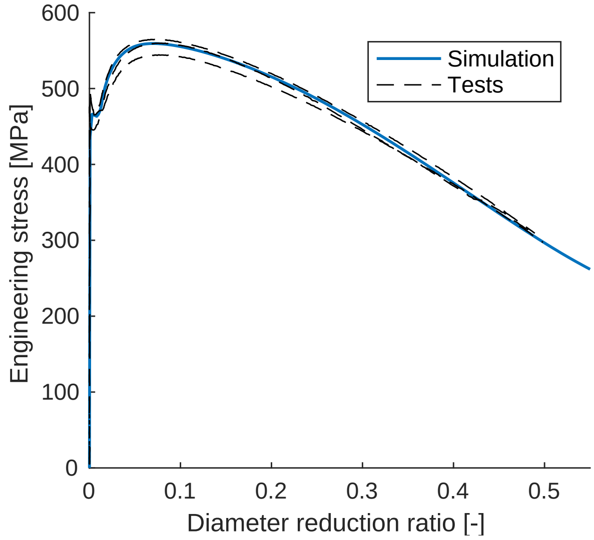

Figure 8: Validation of the matrix yield and work-hardening parameters. Zero initial porosity ($f_0 = 0$) was assumed in the simulation.

3.3.2. Initial void volume fraction

We employed the previously obtained yield and hardening parameters to simulate the notched tensile tests. The notched tensile specimen was modelled using axisymmetric elements with the discretization illustrated in Figure 7b. A suitable value for the initial porosity f_0 was obtained by performing simulations with different values for f_0. The element size applied in the simulations that were used to determine the damage parameters, i.e., f_0 and k_s, was approximately the same as the element size used in the fillet welds of the component test models. This is necessary because the damage parameters are inherently mesh sensitive.

Figure 9a depicts curves of engineering stress (left-hand axis) versus diameter reduction obtained from the tests and simulations conducted with three different initial porosity levels; f_0 = 0.000, 0.001, and 0.002. Additionally, the evolution of the void volume fraction f (right-hand axis) of the critical element in the centre of the specimen is included in the figure. Recall that a critical value for f is not considered in these simulations, and f can therefore grow to unrealistically high values. As can be observed from the figure, the simulations generally over-predict the stress level. This cannot be remedied by the softening of the Gurson model. A possible explanation for the

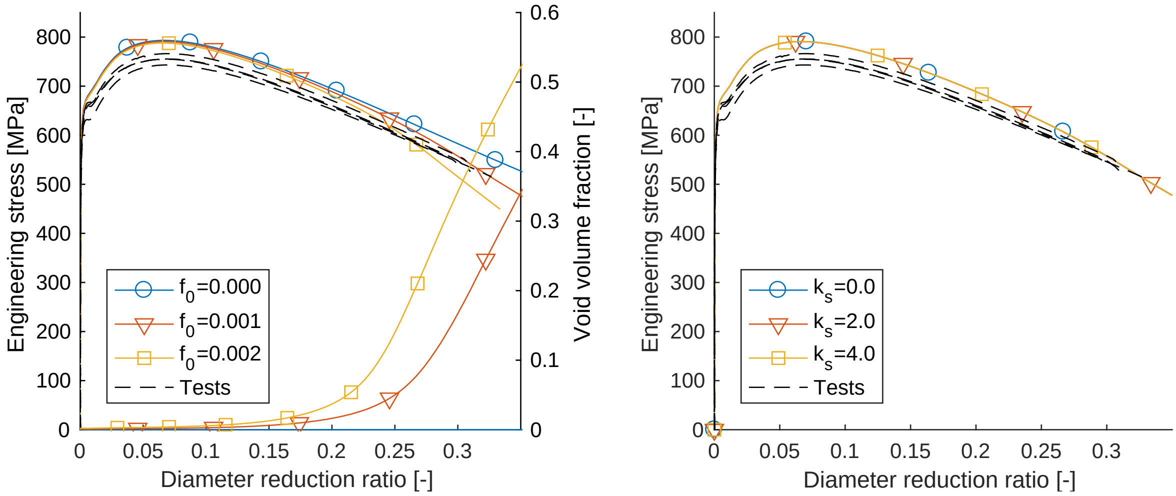

(a) Results with varying f_0 (here k_s = 2.0). **(b)** Results with varying k_s (here f_0 = 0.001).

Figure 9: Curves obtained from simulations and tests with notched specimens. These simulations are used to determine f_0.

discrepancy in stress may be due to pressure sensitivity of the flow stress. Spitzig et al. (1976) and Richmond and Spitzig (1980) found that the yield strengths of steels depended on the hydrostatic pressure. In the more recent works by Wilson (2002) and Bai and Wierzbicki (2008) on aluminium alloys, it is shown that neglecting pressure dependency can lead to over-prediction of the force in simulations of notched tensile tests. Nevertheless, pressure sensitivity of the matrix material is not accounted for in present work. Considering the engineering stress curves in Figure 9a, the initial porosity $f_0 = 0.001$ seems to give an appropriate amount of softening. Moreover, the porosity curves in Figure 9a show that in the simulation with $f_0 = 0.001$, initiation of exponential growth of porosity occurs at a diameter reduction that corresponds well with the diameter reduction at failure in the tests. The initial porosity $f_0 = 0.001$ is therefore adopted in the remaining simulations presented herein. As can be expected for axisymmetric loading conditions, the shear term in Equation (9) has practically no effect on the response, which is demonstrated in Figure 9b.

3.3.3. Shear parameter

A suitable value of the shear parameter k_s was determined from the in-plane shear tests and corresponding simulations. Figure 7c shows the discretized model used in the simulations. The

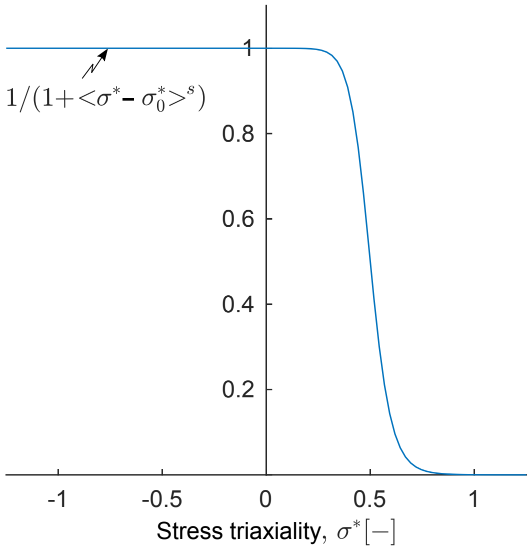

Figure 10: The scaling function of the shear damage contribution in Equation (13) for the chosen values $\sigma_0^* = -0.5$ and $s = 20$.

relative displacement between the two nodes denoted Node 1 and Node 2 in the figure was used as a deformation measure. Digital image correlation was employed to track practically the same points throughout the tests. A similar procedure was utilized by Gruben et al. (2016a,b) for the same type of shear test specimens.

In the simulations of the shear tests, the scaling function of the shear damage contribution in Equation (13) becomes relevant. We chose $\sigma_0^* = -0.5$ and $s = 20$ in the present model, which reduces the shear damage contribution for increasing triaxiality in a similar fashion as suggested by Nielsen and Tvergaard (2010). As shown in Figure 10, these parameters yield virtually no reduction of the shear damage contribution below $\sigma^* = 0.3$, and practically full reduction above $\sigma^* = 0.7$. We verified that the chosen scaling function had minor influence on the response in the shear test simulations, which should be the case because mainly low triaxialities develop in these simulations.

Figure 11 depicts the normalized force-deformation curves obtained from shear tests and simulations, where previously determined material parameters have been employed. Here, the force is normalized with respect to the minimum initial area, i.e., the shear area, of the specimen, whereas the deformation is normalized with respect to the initial distance between the two tracked

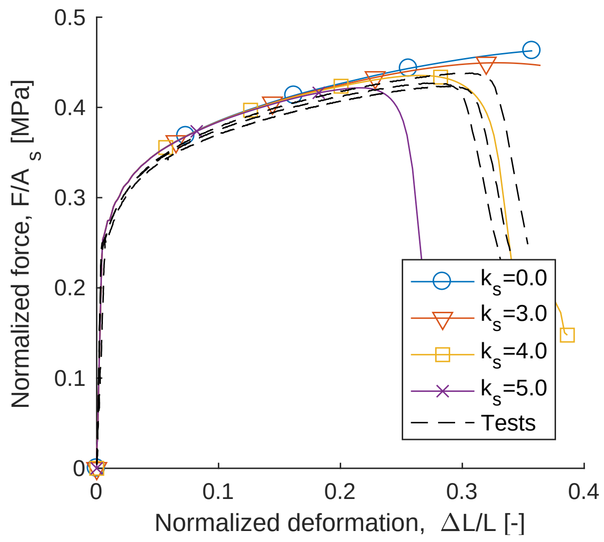

Figure 11: Normalized force vs. normalized deformation obtained from simulations and tests with shear specimens (here $f_0 = 0.001$). These simulations are used to determine k_s.

points/nodes. From these curves we observed that $k_s = 4.0$ produced an adequate prediction of softening and ductile failure progression, and this value is therefore adopted in further simulations. Note that k_s depends on the choice of f_0, and that $k_s = 4.0$ is somewhat high according to Nahshon and Hutchinson (2008), who suggested that this parameter lies in the range $1 < k_s < 3$ for many structural alloys. Note also that using $a = 2$ instead of $a = 6$ in Equation (5), i.e., assuming a von Mises yield surface in the deviatoric stress plane, produced 3-4 % larger over-prediction of the force levels in the simulations of the in-plane shear tests. Thus, accounting for the J_3 dependence of the yield surface is appropriate.

As mentioned, the critical void volume fraction f_c has not been considered in the simulations presented up to this point. Based on the component test simulations, we observed that $f_c = 0.12$ seemed to produce failure at reasonable deformation levels. This value was therefore adopted in all simulations of the component tests, and elements were deleted when their porosity f reached the critical porosity value f_c. Note that the time of failure in the component test simulations was somewhat insensitive to the choice of f_c. This observation is related to the exponential growth of f, causing a rather high increase in porosity for small deformation increments when the damage-induced softening is significant.

3.3.4. Strain-rate parameters

The strain rate parameters $\dot{p}_0$ and c were determined solely from the experimental data acquired from the tensile tests conducted at different strain rates. By using logarithms and neglecting temperature effects, Equation (6) can be rewritten to

$$\log\left(\frac{\sigma_M}{\sigma_0 + \sum_{i=1}^{2} Q_i\left(1 - \exp\left(-\frac{\theta_i}{Q_i}p\right)\right)}\right) = c \cdot \log\left(1 + \frac{\dot{p}}{\dot{p}_0}\right) \tag{16}$$

Figure 12 evaluates the logarithm on the left-hand side of Equation (16) at plastic strains $p = 0.05$ and $p = 0.10$ as a function of the logarithm at the right-hand side of the equation. For such low values of the plastic strain p, the self heating through plastic work is negligible, which justifies neglecting the temperature factor in Equation (6). In Figure 12, a reference plastic strain rate $\dot{p}_0$ of 10^{-3} s^{-1} is used, which is approximately equal to the lowest strain rate in the tests. According to Equation (16), the slopes of the linear curves fitted to the experimental data in Figure 12 provide estimates for the values of c. The average slope of the two curves of each material yielded $c = 0.020$ and $c = 0.017$ for the plate and weld material, respectively, which were used in subsequent simulations.

4. Finite element model of component tests

4.1. Geometry and discretization

Figure 13 displays the FE model of the component tests with the longitudinal specimen. Eight-node brick elements with reduced integration and default hourglass stiffness were used for the entire model. The FE model of the transverse specimen was discretized in a similar fashion. Two symmetry planes were introduced to reduce the number of elements. In the dynamic simulations, the simple representation of the trolley shown in Figure 14 was included. The mass of the trolley model was the same as in the tests, i.e., 1444 kg (without symmetries).

The measured dimensions of the test specimens differed minimally from their nominal dimensions, which are given in Section 2.1. Therefore, the specimens were modelled using the nominal dimensions, except for the throat thickness of the weld of the transverse specimen model. This thickness was set to 4.3 mm because this was the average measured value (the nominal throat thickness was 4.0 mm).

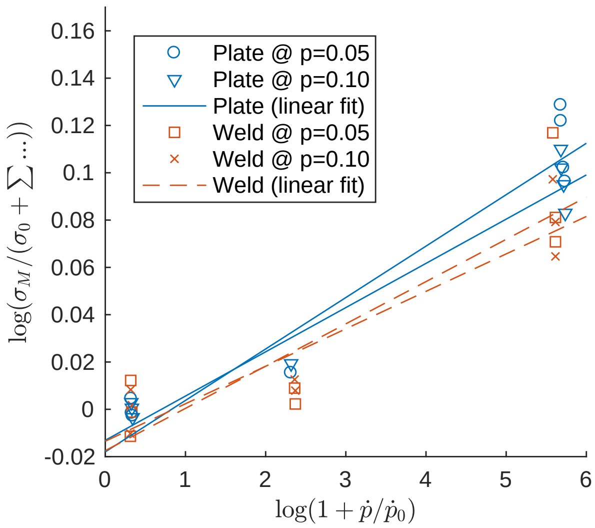

Figure 12: Plot of the left-hand versus right-hand sides of Equation (16) for two values of plastic strain p . The test data was obtained from tensile tests on the weld and plate material performed at different strain rates. Additionally, linear polynomials are fitted to the data so that the slope of these lines represent the strain-rate parameter c according to Equation (16).

Figure 13 also shows the mesh density of the model. The mesh seeds applied to the model were

- 4.0 mm near the bolt hole of the supporting block, and 8.0 mm otherwise for this part.
- 4.0 mm for the bolt and nose.
- 3.0 mm for the plate, except in the vicinity of the weld, where it was 0.75 mm.
- 0.75 mm was also used for the portion of the brick adjacent to the weld, and 2.0 mm was applied otherwise for the brick.
- 0.25 mm was applied to the weld, which corresponds to the element size used in the calibration procedure for the damage parameters.

These mesh seeds resulted in approximately 160 000 elements for the entire model.

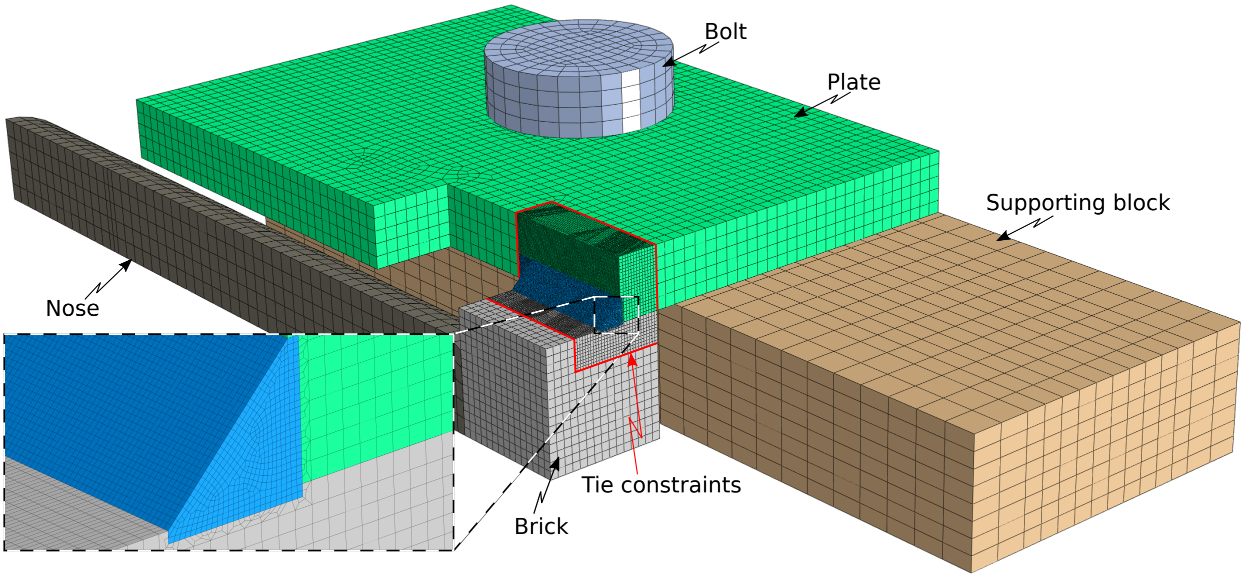

Figure 13: The geometry and discretization of the model of the component tests on longitudinal welds. A quarter of the physical test setup was modelled by exploiting symmetry, i.e., two symmetry planes.

4.2. Contact and constraints

As indicated by the red lines in Figure 13, tie constraints were used in the vicinity of the weld to allow for a sudden transition of mesh density. Care should be shown when applying tie constraints because they do not ensure stress continuity across the constrained boundary. The tie constraints of the model were therefore located at a sufficient distance (7.5-10 mm) from the weld so that they had insignificant effect on the response. In the dynamic simulations, tie constraints

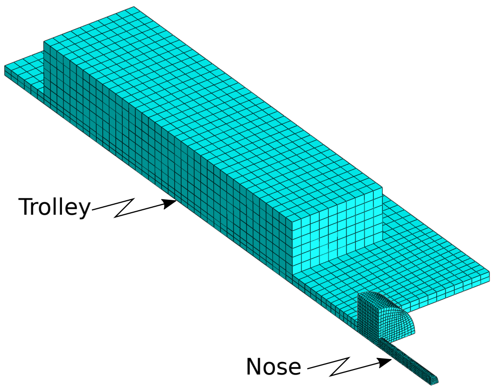

Figure 14: The geometry and discretization of the trolley used in the dynamic simulations.

were also established between the nose and the trolley.

Surface-to-surface contact was defined between appropriate surfaces in the model, namely, nose and brick, plate and brick, plate and support, plate and bolt, and support and bolt. So-called ”hard” contact was used as the contact property in the normal direction of the contact surfaces, and isotropic Coloumb friction with a coefficient of 0.2 was employed in the tangential direction of the surfaces.

4.3. Materials

The materials were modelled as described in Section 3. The constitutive model of the fillet weld was implemented in the FE simulations by a material user subroutine (VUMAT). Figure 15 illustrates how we included the fusion zone of the weld and base materials in the models. The zone stretches from the fusion lines and 0.5 mm into the base materials. This distance of 0.5 mm was based on measurements made on the weld sections shown in Figure 6. The rectangular shape of the fusion zones was used because this simplified meshing the model. Moreover, the fusion zone was assumed to consist of the same material as the fillet weld. As indicated in Figure 15, we ensured initiation of fracture in the weld material by extending the gap between the plate and brick 0.25 mm into the weld material.

As mentioned in Section 3, the materials of the plate and the brick were modelled with von Mises plasticity. This allowed using a built-in material model in Abaqus, which is computationally faster than user subroutines. For these two materials, the flow stress was tabulated as a function of the plastic strain according to the parameters listed in Table 1. We assumed that properties of the plate and brick materials were temperature independent. This assumption is acceptable because these materials experienced only minor to moderate plastic strains in the simulations, and hence insignificant temperature increase.

The nose, bolt, supporting block, and trolley were modelled as elastic materials since these components experienced no plastic deformations in the tests.

In the quasi-static simulations, the materials were assumed strain-rate independent, which is equivalent to setting $c = 0$ in Equation (6). Moreover, isothermal conditions were assumed in the quasi-static simulations, which corresponds to setting $\chi = 0$ in Equation (15). Adiabatic conditions

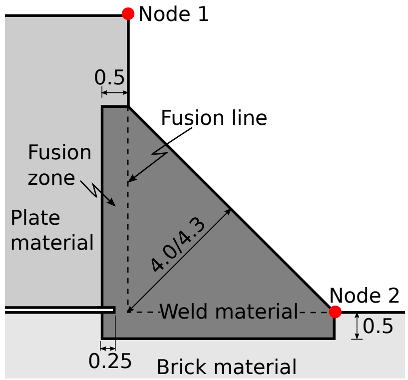

Figure 15: The distribution of the different materials in the vicinity of the weld (measures in mm).

were assumed in the dynamic simulations, and $\chi = 0.9$ was adopted for these simulations, which is a typical value for steels, as reported by Macdougall (2000).

4.4. Boundary and initial conditions

Symmetry conditions were applied to appropriate surfaces in the model. In addition, the end surface of the supporting block closest to the viewpoint in Figure 13 was fixed in all directions.

In the quasi-static simulations, a constant velocity of 0.01 mm/s was applied to the rear surface of the nose. In order to reduce the computational time, selective mass scaling was employed for the quasi-static simulations, and the kinetic energy was verified to be negligible compared to the internal energy. For the dynamic simulations, the trolley was given an initial velocity of 2.4 m/s, which is approximately the initial velocity used in the impact tests.

5. Simulation results

5.1. Quasi-static simulations

Figure 16 displays the force-deformation curves obtained from the quasi-static simulations with both longitudinal and transverse specimens, as well as the results from all replicate quasi-static tests. The relative displacement between the red dots labelled Node 1 and Node 2 in Figure 15 was used as a measure of the deformation of the weld in the simulations. As described by Grimsmo et al. (2017), a comparative deformation measure was used in the tests through digital image correlation. The curves of the tests are plotted up to the instant where one of the welds in

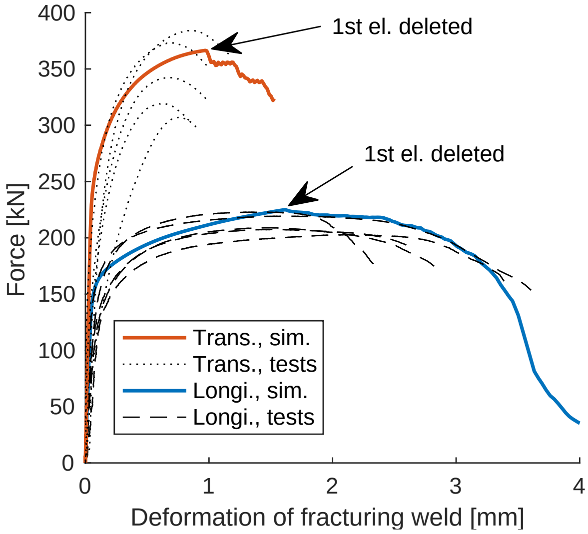

Figure 16: Force-deformation curves obtained from quasi-static simulations and tests.

the specimens failed, which corresponded to when a visible crack had developed along the entire length of the failing weld. Although not shown in Figure 16, this induced a sudden drop in the force in the quasi-static tests. The abscissa in this figure is the deformation of the weld that first fractured, which is relevant for the tests since this weld normally experienced larger deformation than the other welds. In the simulations, the symmetry conditions obviously enforced an identical deformation of the different welds. The appreciable scatter among the experimental curves can be explained by the welds being manufactured manually, which creates inevitable variation in, for instance, size and hardness. A more detailed discussion of the experimental results is given by Grimsmo et al. (2017).

It appears from Figure 16 that the initial stiffness and maximum force (i.e., the resistance) experienced in the tests were faithfully captured by the simulations. Note that the initial stiffness and maximum force of the simulations lie in the upper range of the experimental results. This may be explained by the simulations not capturing the imperfections of the tests such as the asymmetrical deformation of the welds. Considering Figure 16 further, the simulations also seemed to predict initiation of failure at a reasonable deformation level. The apparent softening, i.e., gradual drop in force, observed in Figure 16 occurs due to material softening and element deletion. As mentioned, the tests exhibited a sudden drop in force simultaneously as a full-length crack in the weld appeared. This abrupt drop was not captured properly by the simulations because an incremental erosion of elements occurred rather than the rapid crack growth experienced in the tests. This can be expected since the size of the elements ($\sim$ 0.25 mm) is large compared to the physical crack tip opening. Simulating crack growth using ordinary FE simulations is thus challenging, as shown by for instance Xue et al. (2010) and Gruben et al. (2013). Nevertheless, the current simulations induced a qualitatively similar failure mechanism as experienced in the tests; fracture initiated at the root of the weld and the "crack" propagated outward through the weld and toward the surface at an angle depending on the specimen type, i.e, longitudinal or transverse. Figure 17 displays a good agreement in terms of the angle of the fracture surfaces with respect to the horizontal plane when comparing the tests and simulations. The longitudinal specimens experienced crack propagation with an approximate angle of 45 degrees, whereas the transverse specimens exhibited a less steep fracture angle.

5.2. Dynamic simulations

Compared to the quasi-static simulations, the loading in the dynamic simulations is applied by impact from the trolley shown in Figure 14. Figure 18 displays the force-deformation curves acquired from the dynamic simulations and all replicate dynamic tests. Moreover, the previously presented results from the quasi-static simulations are included in the figure for comparison. In Figure 18, the experimental curves are plotted up to failure, which was defined as the instant the plates of the specimens suddenly moved in the direction opposite to the load direction. This movement indicated a release of elastic strain energy in the plates, which corresponded well with the instant a full-length crack had developed on the surface of at least one of the welds. For the dynamic simulation curves in Figure 18, the arrows labelled "Failure" indicate when the plates started moving in the opposite direction to the load direction. However, this instant did not correspond to when a full-length crack had formed on the surface of the welds in the simulations. This can be explained by the significantly slower crack propagation in the simulations, which was discussed in the previous section.

Since defining the time of failure in the simulations was somewhat ambiguous, care should be shown when comparing the weld deformation at failure obtained from the simulations and the

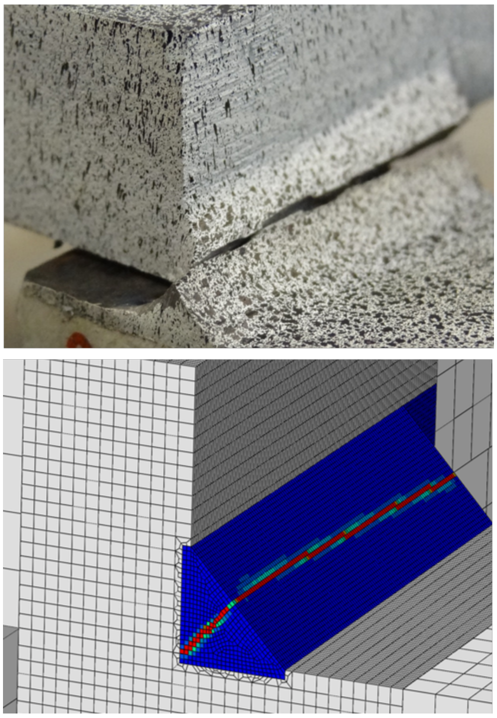

(a) Longitudinal specimen

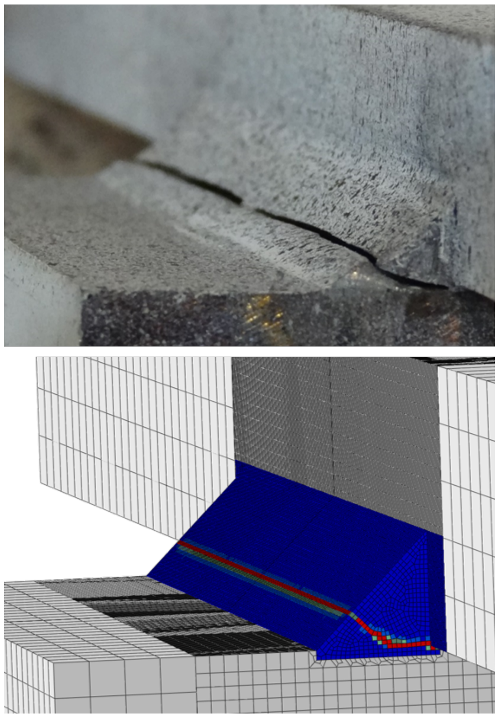

(b) Transverse specimen

Figure 17: Fractured test specimens (top) and fringe plots of the damage superimposed on the undeformed FE models (bottom). The blue elements are undamaged, whereas the red elements reached the critical void volume fraction, and were therefore deleted during the simulations.

tests. Nevertheless, it appears from Figure 18 that the simulations predicted failure at noticeably higher deformation levels than in the tests, particularly for the longitudinal specimens. Grimsmo et al. (2017) showed that the dynamic tests with longitudinal specimens experienced a reduced weld deformation at failure compared to the corresponding quasi-static tests, which was probably due to more localized deformation in the welds. They demonstrated that the enhanced localization was likely caused by self-heating and corresponding thermal softening. Some increase of localization also occurred in the simulations. This is visualized in Figure 19, where the evolution of the equivalent plastic strain p in the first deleted elements is compared for the quasi-static and dynamic simulations with the longitudinal specimen. Note that these two elements are found at the same spatial location in the root of the weld. As observed from the figure, p developed similarly in the two elements up to approximately 0.7 mm weld deformation. Beyond this deformation, how-

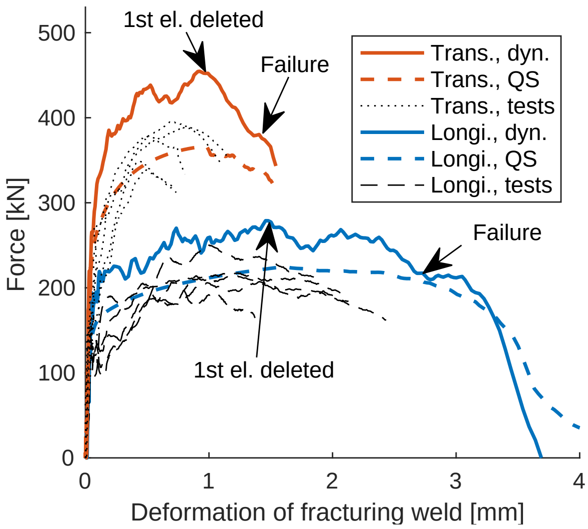

Figure 18: Force-deformation curves obtained from dynamic simulations and tests. The curves from the quasi-static (QS) simulations are included for comparison.

ever, the element originating from the dynamic simulation experienced a more rapidly growing p. Thus, at the same level of weld deformation, the plastic strain p is largest in the element from the dynamic simulation, which indicates an increased localization of deformation for this simulation compared to the quasi-static simulation. Nevertheless, it is possible that the localization in the dynamic simulation is not as significant as in the corresponding tests, which may explain the increased weld deformation at failure in the simulations compared to the tests. Figure 19 shows further that the curves eventually develop a horizontal plateau, which indicates that the elements have reached the critical void content, and have therefore been deleted. Thus, the element from the dynamic simulation failed at a slightly smaller plastic strain than the element from the quasi-static simulation (p_f = 1.34 vs. p_f = 1.39).

Figure 18 clearly shows that the force levels in the dynamic simulations are appreciably greater than in the tests and the quasi-static simulations. Up to maximum force, the difference in force between the dynamic and quasi-static simulations is about 20-25 % for both the longitudinal and transverse specimen cases. This difference can be explained by the high strain rates observed in some of the elements in the welds. The maximum strain rates are of the order of 2000 to 3000 s^{-1}. Such strain rates induce a stress increase of more than 25% in the matrix material

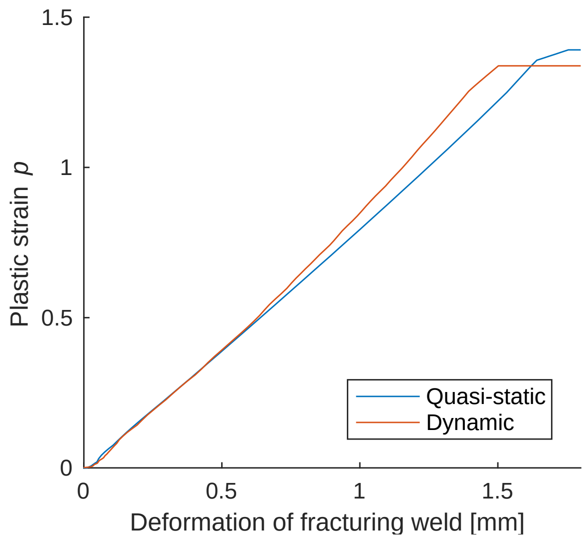

Figure 19: Plastic strain p versus weld deformation acquired from critical elements in the quasi-static and dynamic simulations with the longitudinal specimen. The two elements were located at the same spatial position in the models.

according to Equation (6). The average strain rates at the mid-length cross-section of the welds are approximately 250 and 200 s^{-1} for the longitudinal and transverse specimens, respectively. According to Equation (6), these strain rates correspond to about 23% enhancement of the stress.

Another aspect that affects the force level in the dynamic simulations is the thermal softening factor in Equation (6). However, significant thermal softening was not developed until the late stages of the simulations because the temperature T is governed by the amount of plastic work; see Equation (15). This can be observed by comparing the curves of the dynamic and quasi-static simulations in Figure 18. For instance, the difference between the two types of simulations is noticeably reduced after about 2 mm weld deformation for the longitudinal specimen case. The elements that were deleted in the dynamic simulations typically reached a temperature of approximately 330 °C. This corresponds to a thermal softening of 22 % according to Equation (6). It should be mentioned that using a finer mesh, and adjusting the damage parameters accordingly, would allow greater plastic strains to develop in the elements before deletion. In turn, this would induce higher temperatures in the simulations.

The discrepancies between simulations and tests in terms of force and weld deformation at failure may be due to excessive strain-rate hardening or insufficient thermal softening in the simulations. This is discussed in more detail in the subsequent section. The discrepancies may also be due to the material model being unable to describe the material response sufficiently accurate. For instance, the strain rates vary considerably both spatially within the welds and temporally during the deformation; the strain rates range between approximately 10 and 3000 s^{-1}. Considering the results from the strain-rate investigation in Figure 12, we can observe that the employed material model appears inaccurate for certain strain rates. Specifically, the material model may predict too high flow stresses for medium strain rates. This may have contributed to the over-prediction of force levels seen in Figure 18. Huh et al. (2014) discuss how the Johnson-Cook model can be inaccurate for steels subjected to varying strain rates, and that other models can be better suited for steels. Another possible explanation for the discrepancies of force levels in Figure 18 may be that the element sizes used in the models are not sufficiently fine. However, we ran simulations with finer element meshes (approx. 40% reduction of the element size in the weld and in the base material in the vicinity of the weld), and the maximum forces in these simulations differed only slightly from the maximum forces in the simulations presented herein. This issue was therefore not pursued further.

5.3. Effect of varying strain rate and temperature sensitivity

The strain-rate parameter c was determined equal to 0.017 from tests performed on the butt weld material, and this value was adopted for the fillet weld material. However, according to the tension test results presented in Figure 5, the fillet weld material is around 20% stronger than the butt weld material. This difference in strength was attributed to the different thermal histories during manufacturing of the two weld types. Børvik et al. (2009) found $c = 0.0166$ for Weldox 400 E steel, and $c = 0.0098$ for Weldox 700 E steel, where the specified minimum yield strengths are indicated by the digits in the alloy designations. The major difference between these two steels during manufacturing is the heat treatment. Analogously, the fillet weld material has possibly a lower c than the butt weld material. We therefore ran dynamic simulations with $c = 0.010$ and $c = 0.0$ for the weld material to investigate how the strain-rate hardening affected the response, and the result is displayed in Figure 20a. Clearly, decreasing the strain-rate parameter c reduces the

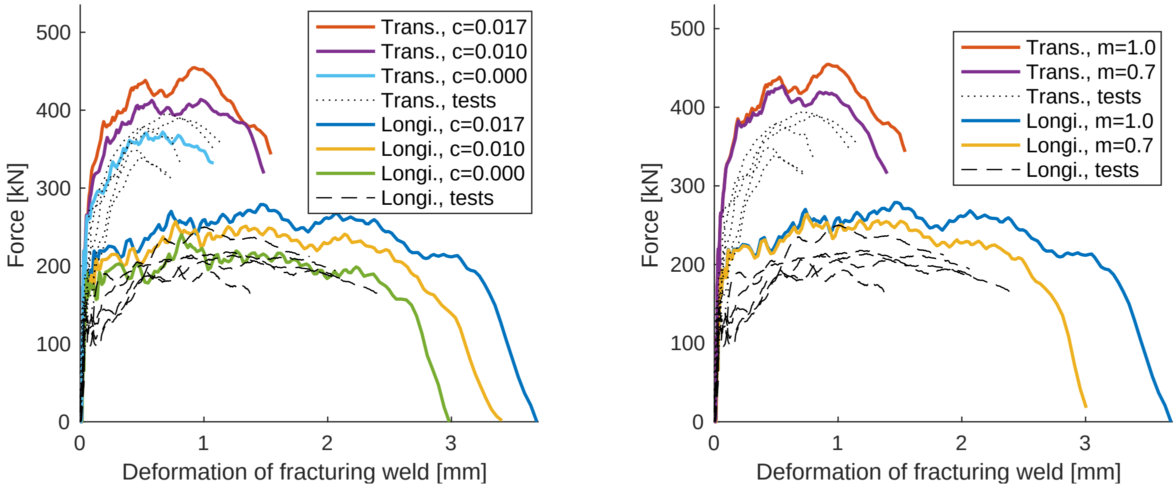

(a) Effect of reducing the strain-rate parameter c from 0.017 to 0.010 and 0.000.

(b) Effect of reducing the temperature parameter m from 1.0 to 0.7.

Figure 20: Force-deformation curves obtained from dynamic simulations where the strain-rate and temperature sensitivity were varied.

force and the weld deformation at failure for both the longitudinal and transverse specimens. The reduced weld deformation at failure occurred because the decreased strain-rate hardening allowed increased localized deformation in the weld.

The temperature parameter m introduced in Equation (6) was assumed equal to 1.0 in the previous simulations, which was based on tests of different Weldox steels performed by Dey et al. (2004). However, Xu and Li (2009) found $m = 0.7$ from tests on a steel weld material with a similar strength to the weld material used in the present work. A lower value for m increases the thermal softening. We therefore investigated the effect of reducing m to 0.7 in the dynamic simulations. Figure 20b shows that the increased thermal softening effect introduced by reducing m is only visible after a considerable amount of weld deformation, which corresponds to the observations in Section 5.2. As can be expected, the increased thermal softening reduces the weld deformation at failure.

The results in Figure 20 suggest that the force levels and weld deformations at failure in the dynamic simulations may be somewhat reduced compared to the results presented in Figure 18.

Nevertheless, the discrepancies observed between dynamic tests and simulations are possibly due to the models not being able to capture all mechanisms occurring in the dynamic tests, which may be because of discretization issues.

5.4. Comparison with uncoupled damage model

The shear-modified Gurson model employed herein is a relatively complex model that requires at least three types of material tests for calibration of the material parameters. It is therefore interesting to investigate whether a simpler model is able to capture the response experienced in the tests. In this investigation, we chose a material model where the damage is uncoupled from the constitutive relations. The initial void volume fraction f_0 was set to zero. Thus, the Gurson yield function was reduced to a Hershey yield function, i.e., $f \equiv 0$ in Equation (4). The material was still assumed elastic-thermoviscoplastic, i.e., the constitutive relation in Equation (6) was retained. The damage D in the material was calculated by means of the failure criterion proposed by Cockcroft and Latham (1968), viz.

$$D = \frac{1}{W_c} \int_0^p \langle \sigma_I \rangle \mathrm{d}p \tag{17}$$

where σ_I is the maximum principal stress and the failure parameter W_c is a constant. Since the principal stresses can be expressed as functions of the stress triaxiality and the Lode angle, the Cockcroft-Latham criterion is implicitly dependent on these two stress invariants. Bai and Wierzbicki (2015) provide the fracture loci obtained from the shear-modified Gurson model and the Cockcroft-Latham criterion. In the simulations presented herein, the elements are deleted as the integral in Equation (17) reaches the value W_c at the integration points. By following the procedure described by Grimsmo et al. (2016), W_c was determined to be 940 MPa from the smooth tension test of the fillet weld material.

Figure 21 plots the force-deformation curves acquired by employing the Cockcroft-Latham (CL) failure model, as well as the previously presented curves obtained with the shear-modified Gurson (MG) model. As observed from the figure, the two material models produce practically an identical response up to approximately maximum force. This implies that the softening originating from void growth in the Gurson model has negligible influence prior to maximum force is reached. Considering the curves of the transverse specimen in Figure 21a, the CL model seems to predict

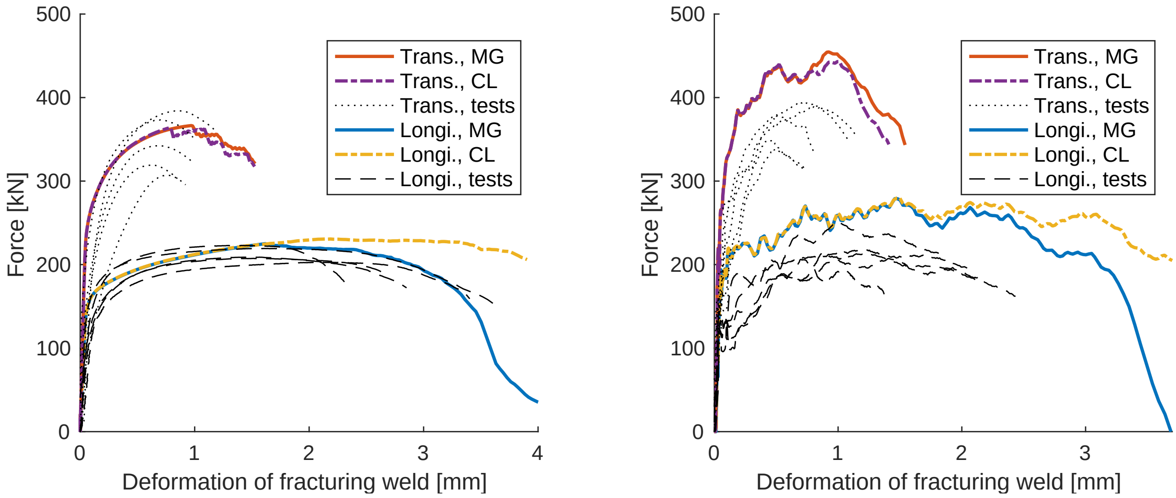

(a) Quasi-static simulation and test results **(b)** Dynamic simulation and test results

Figure 21: Force-deformation curves obtained from quasi-static and dynamic simulations with the shear-modified Gurson (MG) and Cockcroft-Latham (CL) damage models.

failure at a reasonable weld deformation. However, the CL model produces initiation of failure at somewhat smaller weld deformation than the MG model, and the force-deformation curve after maximum force has a more protruding step-like shape. Furthermore, Figure 21a displays that the CL model is unable to predict failure at the correct weld deformation for the longitudinal specimen. The explanation may be that a shear type of loading is dominating at the failure plane of the longitudinal specimens, and the failure parameter W_c in Equation (17) was calibrated from tension tests. On the other hand, a combined shear and tension type of loading occurs at the failure plane of the transverse specimens. The dynamic simulations displayed similar tendencies as the quasi-static simulations, as shown in Figure 21b.

Compared to the simulations with the Cockcroft-Latham criterion, better agreement with the tests would probably be obtained by employing, for instance, the extended Cockcoft-Latham criterion proposed by Gruben et al. (2012). The extended version enables explicitly accounting for the Lode dependency of failure, but requires more tests for calibration.

6. Concluding remarks

FE simulations of previous quasi-static and dynamic (impact) tests of fillet welds have been conducted. The test specimens consisted of structural steel parts that were joined by either longitudinal or transverse fillet welds. A shear-modified Gurson model, heuristically extended to accommodate effects of the third principal invariant of the stress deviator, was employed to account for material damage and subsequent fracture in the welds. Additionally, strain rate and temperature dependencies were included in the dynamic simulations. The majority of the material constants entering the constitutive model was determined from a series of material tests, including smooth and notched tensile specimens, and in-plane simple shear tests. The remaining material parameters were adopted from appropriate literature.

The behaviour in terms of force versus weld deformation experienced in the quasi-static tests was well captured by the simulations, both with longitudinal and transverse welds. In the simulations of the quasi-static tests, failure initiated at reasonable weld deformations, and the cracks propagated at angles similar as in the tests. However, the simulations were unable to capture the rapid crack growth occurring in the late stages of the quasi-static tests. A more refined spatial discretization is probably necessary to be able to simulate this crack growth.

In the simulations of the dynamic tests, a considerable overestimation of the force levels and weld deformations at failure was observed. Due to uncertainties with respect to the material parameters governing the strain-rate hardening and thermal softening, the force and deformation levels should possibly be moderately reduced, as was demonstrated by parameter studies.

Finally, we conducted a comparison of the simulation results obtained with the shear-modified Gurson model and a simpler material model, where the damage description was uncoupled from the constitutive equations. The Gurson model produced generally a better agreement with the tests, particularly for the simulations with longitudinal specimen, where loading of the welds occurs predominantly by shearing.

Acknowledgements

The work has received economical support from the Research Council of Norway through the SFI scheme. Grant number: 237885. We thank Assoc. Prof. D. Morin for implementing the VUMAT in Abaqus.

References

Bai, Y., Wierzbicki, T., 2008. A new model of metal plasticity and fracture with pressure and lode dependence. Int J Plasticity 24 (6), 1071–1096.

Bai, Y., Wierzbicki, T., 2015. A comparative study of three groups of ductile fracture loci in the 3d space. Eng Frac Mech 135, 147 – 167.

Børvik, T., Dey, S., Clausen, A., 2009. Perforation resistance of five different high-strength steel plates subjected to small-arms projectiles. Intl J of Impact Eng 36 (7), 948–964.

Børvik, T., Hopperstad, O., Berstad, T., Langseth, M., 2001. A computational model of viscoplasticity and ductile damage for impact and penetration. Eur J Mech A/Solids 20 (5), 685–712.

Cockcroft, M., Latham, D., 1968. Ductility and the workability of metals. J Inst Metals 96 (1), 33–39.

Dey, S., Børvik, T., Hopperstad, O., Leinum, J., Langseth, M., 2004. The effect of target strength on the perforation of steel plates using three different projectile nose shapes. Int J of Impact Eng 30 (8), 1005–1038.

Doege, E., Seibert, D., 1995. Prediction of necking and wrinkling in sheet-metal forming. J Mater Process Tech 50, 197–206.

Garrison, W., Moody, N. R., 1987. Ductile Fracture. J Phys Chem Solids 48 (11), 1035–1074.

Grimsmo, E., Clausen, A., Aalberg, A., Langseth, M., 2016. A numerical study of beam-to-column joints subjected to impact. Eng Struct 120, 103–115.

Grimsmo, E., Clausen, A., Aalberg, A., Langseth, M., 2017. Fillet welds subjected to impact loading - an experimental study. In press in Int J Impact Eng.
URL `https://doi.org/10.1016/j.ijimpeng.2017.02.023`

Gruben, G., Hopperstad, O., Børvik, T., 2012. Evaluation of uncoupled ductile fracture criteria for the dual-phase steel docol 600dl. Int J Mech Sci 62 (1), 133–146.

Gruben, G., Hopperstad, O. S., Børvik, T., 2013. Simulation of ductile crack propagation in dual-phase steel. Int J Fracture 180 (1), 1–22.

Gruben, G., Langseth, M., Fagerholt, E., Hopperstad, O. S., 2016a. Low-velocity impact on high-strength steel sheets: An experimental and numerical study. Int J of Impact Eng 88, 153–171.

Gruben, G., Morin, D., Langseth, M., Hopperstad, O., 2016b. Strain localization and ductile fracture in advanced high-strength steel sheets. Eur J of Mech A/Solids 61, 315–329.

Gurson, A., 1977. Continuum Theory of Ductile Rupture by Void Nucelation and Growth: Part I – Yield Criteria and Flow Rules for Porous Ductile Media. J Eng Mater Tech 99 (1), 2–15.

Hershey, A. V., 1954. The plasticity of an isotropic aggregate of anisotropic face-centered cubic crystals. J Applied Mech 21 (3), 241–249.

Hill, R., 1948. A theory of the yielding and plastic flow of anisotropic metals. In: Proceedings of the Royal Society of London. Series A, Mathematical and Physical Sciences. Vol. 193.

Hosford, W. F., Caddell, R. M., 1993. Metal forming: mechanics and metallurgy (second edition). PTR Prentice Hall, Upper Saddle River, NJ 07458, USA.

Huh, H., Ahn, K., Lim, J. H., Kim, H. W., Park, L. J., 2014. Evaluation of dynamic hardening models for bcc, fcc, and hcp metals at a wide range of strain rates. J Mat Proc Tech 214 (7), 1326 – 1340.

Johnson, G. R., Cook, W. H., 1983. A constitutive model and data for metals subjected to large strains, high strain rates and high temperatures. In: Proceedings of the 7th International Symposium on Ballistics. Vol. 21. The Hague, The Netherlands, pp. 541–547.

Kanvinde, A., Fell, B., Gomez, I., Roberts, M., 2008. Predicting fracture in structural fillet welds using traditional and micromechanical fracture models. Eng Struct 30 (11), 3325 – 3335.

Kanvinde, A., Gomez, I., Roberts, M., Fell, B., Grondin, G., 2009. Strength and ductility of fillet welds with transverse root notch. J Constr Steel Res 65 (4), 948 – 958.

Macdougall, D., 2000. Determination of the plastic work converted to heat using radiometry. Exp Mech 40 (3), 298–306.

Miazga, G. S., Kennedy, D. L., 1989. Behaviour of fillet welds as a function of the angle of loading. Can J Civil Eng 16 (4), 583–599.

Nahshon, K., Hutchinson, J. W., 2008. Modification of the Gurson Model for shear failure. Eur J Mech A/Solids 27 (1), 1–17.

Nielsen, K. L., Tvergaard, V., 2010. Ductile shear failure or plug failure of spot welds modelled by modified gurson model. Eng Fracture Mech 77 (7), 1031 – 1047.

Picòn, R., Cañas, J., 2009. On strength criteria of fillet welds. Int J Mech Sci 51 (8), 609 – 618.

Richmond, O., Spitzig, W., 1980. Pressure dependence and dilatancy of plastic flow. Theoretical Appl Mech, 377–386.

Ristinmaa, M., Ottosen, N. S., 2000. Consequences of dynamic yield surface in viscoplasticity. Int J Solids Struct 37 (33), 4601–4622.

Spitzig, W. A., Sober, R. J., Richmond, O., 1976. The effect of hydrostatic pressure on the deformation behavior of maraging and hy-80 steels and its implications for plasticity theory. Metallurgical Transactions A 7 (11), 1703–1710.

Tvergaard, V., 1981. Influence of voids on shear band instabilities under plane strain conditions. Int J Fracture 17 (4), 389–407.

Wilson, C. D., 2002. A critical reexamination of classical metal plasticity. Transactions - ASME, J Appl Mech 69 (1), 63–68.

Xu, Z., Li, Y., 2009. Dynamic behaviors of 0cr18ni10ti stainless steel welded joints at elevated temperatures and high strain rates. Mech Mater 41 (2), 121–130.

Xue, L., 2008. Constitutive modeling of void shearing effect in ductile fracture of porous materials. Eng Fracture Mech 75 (11), 3343–3366.

Xue, Z., Faleskog, J., Hutchinson, J. W., 2013. Tension–torsion fracture experiments–part ii: Simulations with the extended gurson model and a ductile fracture criterion based on plastic strain. Int J Solids Struct 50 (25), 4258–4269.

Xue, Z., Pontin, M. G., Zok, F. W., Hutchinson, J. W., 2010. Calibration procedures for a computational model of ductile fracture. Eng Fracture Mech 77 (3), 492–509.